AIAA JOURNAL
Vol. 41, No. 4, April 2003

Toward a Flame Embedding Model for Turbulent Combustion Simulation

Y. M. Marzouk* and A. F. Ghoniem†
Massachusetts Institute of Technology, Cambridge, Massachusetts 02139
and
H. N. Najm‡
Sandia National Laboratories, Livermore, California 94551

Combustion in turbulent flows may take the form of a thin flame wrapped around vortical structures. For this regime, the flame embedding approach seeks to decouple computations of the "outer" nonreacting flow and the combustion zone by discretizing the flame surface into a number of elemental flames, each incorporating the local impact of unsteady flow–flame interaction. An unsteady strained laminar flame solver, based on a boundary-layer approximation of combustion in a time-dependent stagnation-point potential flow, is proposed as an elemental flame model. To validate the concept, two-dimensional simulations of premixed flame–vortex interactions are performed for a matrix of vortex strengths and length scales, and a section of the flame is selected for comparison with the flame embedding model results. Results show that using the flame leading-edge strain rate gives reasonable agreement in the cases of low strain rate and weak strain rate gradient within the flame structure. This agreement deteriorates substantially when both are high. We propose two different schemes, both based on averaging the strain rate across the flame structure, and demonstrate that agreement between the one-dimensional model and the two-dimensional simulation greatly improves when the actual strain rate at the reaction zone of the one-dimensional flame is made to match that of the two-dimensional flame.

Introduction

NUMERICAL simulation of multidimensional turbulent reacting flow is a computationally expensive undertaking, posing the challenge of integrating the unsteady reacting Navier–Stokes equations, coupled with multispecies transport and detailed chemical kinetics, over a wide spectrum of length scales and timescales. Although it is possible to perform such simulations for a number of idealized problems in small domains, this approach is likely to remain prohibitive for reacting flows in engineering systems.

For many reacting flows of practical interest, however, the combustion zone may take the form of a thin flame surface wrapped around vortical structures.[1] In this regime of turbulent combustion, corresponding to Damköhler number $Da \gg 1$ and Karlovitz number $Ka \leq 1$, the flame occupies only a fraction of the total flow volume. Motivated by these scaling considerations, the flamelet concept, which models the flame surface as an ensemble of asymptotically thin flames that respond instantaneously to the local strain rate, was introduced.[2,3] Burning parameters for these flamelets can be tabulated offline as functions of strain rate or scalar dissipation and mixture composition, and hence, the transport and kinetic equations of reacting flow, with their corresponding length scales and timescales, need not be integrated over the course of a simulation.

The assumptions underlying the flamelet concept, however, pose certain limitations on its applicability. Numerous computational[4–13] and experimental[14,15] studies of laminar flames, as well as recent detailed numerical simulations of reacting flow,[16–18] point to the importance of unsteady flame response in a turbulent environment in which flow timescales are short. Many studies have stressed the importance of detailed chemistry and species transport in predicting dynamic flame response.[4–6,16–18] Simulations of flame–vortex interaction,[16,17] for example, have shown that a flame may survive at strain rates higher than the static extinction value if these strain rates occur over short durations and that pocket formation and reconnection of the flame surface may occur.[19–21] Unsteady effects change the ignition and extinction characteristics of flames from those observed under steady flow conditions; indeed, extinction and reignition are commonly observed in reacting flows with high shear rates. Moreover, unsteadiness has been shown to be significant in capturing the results of flame surface folding and interactions between neighboring flames.[19,20,22]

The flame embedding approach seeks to relax some of the idealizations of flamelet modeling and, thus, extend its applicability, particularly in the context of large-eddy simulations. In this approach, the local structure of the combustion zone is assumed to be that of a flame subject to time-varying strain rate and possibly time-varying curvature. Scalar profiles within the flame are assumed to be locally one-dimensional in the direction normal to the flame surface. Thus, the effect of strain on the flame surface is modeled with a traditional stagnation-flow flame configuration[23] but with a time-varying characteristic strain rate. To pursue this approach within a large-eddy simulation, it is necessary to track a flame surrogate—that is, a surface representing the interface between reactants and products or between fuel and oxidizer. This surface is divided into segments; each segment is considered an elemental flame whose structure is modeled by the strained flame calculations. The similarity between this approach and flamelet approaches lies in that both treat the combustion zone as an ensemble of locally one-dimensional flames. In the flame embedding approach, however, we retain the unsteadiness of the interactions and, hence, preserve the impact of the Lagrangian flow history on combustion. Each elemental flame structure calculation is performed separately using the strain rate, curvature, and mixture composition computed along its trajectory. Thus, the flame embedding approach should be able to account for many forms of unsteady flow–flame interaction, including unsteadiness resulting from mixing and mixture nonuniformity.[24,25]

Initial efforts at flame embedding[26–28] centered on simulations of a two-dimensional reacting shear layer, decomposing the flow into a nonreacting outer flow and an inner combustion zone within

Presented as Paper 2000-0866 at the AIAA 38th Aerospace Sciences Meeting, Reno, NV, 10–13 January 2000; received 5 March 2002; revision received 4 October 2002; accepted for publication 7 October 2002.

*Research Assistant, Department of Mechanical Engineering. Member AIAA.
†Professor, Department of Mechanical Engineering. Associate Fellow AIAA.
‡Principal Member of the Technical Staff, Combustion Research Facility.

which transport and reaction occur, as described earlier. An elemental flame model, essentially a subgrid model for the combustion zone, captures the dynamic effects of strain rate imposed by the flow on the flame surface, whereas the flame acts as a source of volumetric expansion and baroclinic vorticity on the outer flow. Outer and inner solutions, to borrow the terminology of asymptotic expansions, are thus dynamically and kinematically linked. These earlier developments made use of single-step or reduced kinetic models and introduced simplifying assumptions for species transport and for the evaluation of the "effective" strain rate acting on the flame structure.

This paper advances the state of the art in two ways. First, we present an unsteady elemental flame model incorporating detailed kinetics and transport. The model takes the familiar form of a flame strained by unsteady stagnation-point potential flow,[4,5] but in comparison with earlier studies, we emphasize particular features of the formulation that emerge when the external potential flow is parameterized by a time-varying strain rate $a(t)$. In particular, we examine different choices for how to extract or estimate the value of $a(t)$, given a strain rate distribution in a multidimensional reacting flow for which flow dynamic gradients may be of the same order of magnitude as the flame structure gradients. These features prove important when calculating the Lagrangian strain rate history of an elemental flame over the course of a flame embedding simulation. Moreover, we implement a powerful set of techniques for numerical solution of the unsteady strained flame model, designed to address the stiffness of detailed chemistry and to compute flame structures more efficiently and robustly over a wide parameter range of mixture and flow transients. The numerical treatment is validated by spatial and temporal resolution studies and by comparison with a well-benchmarked steady-state flame solution.

Our second objective is to examine the validity of the flame embedding approach via comparison with detailed simulations of flame–vortex interaction, using the latter as a representative, canonical problem of turbulent combustion.[29] Two-dimensional simulations of a premixed flame interacting with a vortex pair are performed for a matrix of length scales and timescales, characterized by vortex size, circulation, and vortex pair separation. In each of these simulations, a section of the flame surface is then selected for comparison with the flame embedding approach. We extract the Lagrangian history of flow conditions local to the flame element and use this history as an input to the elemental flame model. The impact of the unsteady flow on heat release rate and flame structure, as observed in the flame–vortex interactions, is then compared to that predicted by the one-dimensional elemental flame.

In seeking to model a flame surface in two or three dimensions with one-dimensional elemental flames, a validation study of the flame embedding approach, as described earlier, must necessarily address issues of scaling. Certain choices of the vortex pair parameters may place the flow–combustion interactions outside the regime where the flame surface may be considered asymptotically thin with respect to flow length scales. Indeed, for certain values of the vortex pair parameters, we observe that the tangential strain rate exerted by the vortices on the flame may vary significantly through the flame thickness. Yet, a one-dimensional model of the flame structure may still be applicable.[29] This observation motivates a crucial question: how to define the elemental flame model's strain rate parameter $a(t)$ when extracting a Lagrangian strain rate history from the multidimensional flow. We construct three different schemes for this purpose and compare the heat release rates thus obtained. In the process, we further elucidate the applicable regime of the flame embedding model, in terms of flame thickness with respect to flow length scales.

Model Formulation

The flame strained in a stagnation point flow has long been proposed as a subgrid model for turbulent combustion in the flamelet regime,[4–10] combustion in which the flame surface is thin, continuous, and wrinkled by vortical structures. We use this model here but allow the strain rate to vary as a function of time, to capture the physics of unsteady flame response described earlier. (The flame model presented in this paper does not incorporate the effects of curvature on the flame surface. This development is left to future work.) This model is labeled the elemental flame,[10,28] to emphasize its use in a Lagrangian discretization of the flame surface, distinguishing it from the conventional quasi-steady flamelet approach used in closure modeling.

One-dimensional governing equations for the elemental flame are obtained as follows. A boundary-layer approximation is applied across the flame, and a solution is considered along the stagnation streamline, $x = 0$; y is the coordinate normal to the flame surface. The outer flow, a stagnation-point potential flow with velocity field $u_{-\infty} = a(t)x$ and $v_{-\infty} = -(j+1)a(t)y$, yields the pressure gradient as a function of the imposed strain rate:

$$\frac{\partial p}{\partial x} = -\rho_u u_{-\infty} a - \rho_u \frac{u_{-\infty}}{a}\frac{\mathrm{d}a}{\mathrm{d}t} \tag{1}$$

Note that $j = 0$ for a planar flow and $j = 1$ for an axisymmetric flow, in which case r may be substituted for x in the given expressions. The notation ρ_u in Eq. (1) emphasizes that the density of the unburned mixture is used to define the pressure gradient. If the densities of both incoming streams are equal, $\rho_u = \rho_{-\infty} = \rho_\infty$, this distinction is moot. In the premixed flame, however, expansion resulting from heat release within the flame requires a products-side stream entering with lower density and, to maintain a constant pressure gradient, a higher effective strain rate. Defining the strain rate parameter $a(t)$ on the unburned side, in accordance with the expression for the given pressure gradient thus ensures consistency across all flame configurations.

Introducing the similarity variable $U \equiv u/u_{-\infty}$ and the notation $V \equiv \rho v$, and substituting the pressure gradient expression into the equation for momentum conservation inside the boundary layer, we obtain the following equations for species, energy, momentum, and mass conservation, respectively:

$$\rho\frac{\partial Y_k}{\partial t} + V\frac{\partial Y_k}{\partial y} + \frac{\partial}{\partial y}(\rho Y_k \mathcal{V}_k) - \dot{w}_k W_k = 0 \tag{2}$$

$$\rho\frac{\partial T}{\partial t} + V\frac{\partial T}{\partial y} - \frac{1}{c_p}\frac{\partial}{\partial y}\left(\lambda\frac{\partial T}{\partial y}\right) + \frac{1}{c_p}\left(\sum_k^K \rho c_{p,k} Y_k \mathcal{V}_k\right)\frac{\partial T}{\partial y} + \frac{1}{c_p}\sum_k^K \dot{w}_k H_k = 0 \tag{3}$$

$$\rho\frac{\partial U}{\partial t} + \rho U\frac{1}{a}\frac{\mathrm{d}a}{\mathrm{d}t} + \rho U^2 a + V\frac{\partial U}{\partial y} - \frac{\partial}{\partial y}\left(\mu\frac{\partial U}{\partial y}\right) - \rho_u\left(\frac{1}{a}\frac{\mathrm{d}a}{\mathrm{d}t} + a\right) = 0 \tag{4}$$

$$\frac{\partial \rho}{\partial t} + \frac{\partial V}{\partial y} + (j+1)\rho U a = 0 \tag{5}$$

where the diffusion velocity is

$$\mathcal{V}_k = -\frac{1}{X_k} D_{km}\frac{\partial X_k}{\partial y} \tag{6}$$

and the mixture-averaged diffusion coefficient D_{km} is defined in terms of binary diffusion coefficients $\mathcal{D}_{jk}$ as[23]

$$D_{km} = (1 - Y_k)\Bigg/\sum_{j\neq k}^K \frac{X_j}{\mathcal{D}_{jk}} \tag{7}$$

Here Y_k is the mass fraction of species k and W_k and $\dot{w}_k$ are the molar weight and molar production rate, respectively. In the remaining equations, c_p is the specific heat of the mixture, λ is the thermal conductivity, H_k is the molar enthalpy of the kth species, ρ_u is the density of the reactants mixture, and μ is the dynamic viscosity of the mixture. Note that thermal diffusion velocities are neglected. The low-Mach-number assumption has been employed, and hence, density is calculated as a function of the temperature, species mass fractions, and the spatially uniform thermodynamic pressure via the ideal gas equation of state.

Whereas the velocity u is zero along the stagnation streamline, the momentum equation (4) in U is retained to govern variation of the strain rate through the flame, where, by definition,

$$aU = \left.\frac{\partial u}{\partial x}\right|_{x=0} \tag{8}$$

yields the strain rate profile.

Boundary conditions for the species and energy equations consist of defining the composition and temperature of the two incoming streams of the stagnation-point flow:

$$y = \pm\infty: \quad Y_k = Y_{k,\pm\infty}(t),\ T = T_{\pm\infty}(t) \tag{9}$$

The continuity equation requires only one boundary condition; typically, this boundary condition would specify zero velocity at the stagnation point, $V(y=0)=0$. Numerical considerations discussed in the next section, however, suggest that we impose a boundary condition at $y=-\infty$ and leave the stagnation-point definition to fix the origin of the y axis.

The momentum conservation equation requires two boundary conditions. At an unburned stream, $u=u_{-\infty}$, and so the boundary condition is by definition $U=1$. Setting the spatial gradients in Eq. (4) to zero yields an ordinary differential equation (ODE) for U at the burned-stream boundary, denoted by U_b:

$$\frac{\mathrm{d}U_b}{\mathrm{d}t} = -U_b^2 a - U_b\left(\frac{1}{a}\frac{\mathrm{d}a}{\mathrm{d}t}\right) + \frac{\rho_u}{\rho_b}\left(\frac{1}{a}\frac{\mathrm{d}a}{\mathrm{d}t} + a\right) \tag{10}$$

Here ρ_b is the density of the burned mixture. For a premixed flame, the strain rate in the incoming products-side mixture thus responds dynamically to the imposed strain rate. This far-field boundary condition also places an important requirement on the size of the computational domain; the flame must be far enough from the $+\infty$ and $-\infty$ boundaries for spatial gradients in U to vanish. In the case of steady strain rate, the burned-stream boundary condition on U reduces to

$$U_b = \sqrt{\rho_u/\rho_b} \tag{11}$$

To accurately characterize flame structure and response, detailed transport and chemistry are used to evaluate transport coefficients and reaction terms in the model. Transport properties μ, λ, and D_{km} are evaluated using Sandia's TRANSPORT libraries.[30] Chemical source terms and mixture properties are evaluated using CHEMKIN.[31] We use a C_1 kinetic model for methane–air combustion,[32] consisting of 46 reactions among 16 species.

It is worthwhile to piont out those aspects of the present formulation that differ from earlier treatments of the strained flame in unsteady stagnation point potential flow. In contrast with Darabiha,[5] we retain the unsteady term $-\rho_u x(\mathrm{d}a/\mathrm{d}t)$ in the pressure gradient expression (1) and, thus, the corresponding $1/a(\mathrm{d}a/\mathrm{d}t)$ terms in the momentum equation (4) and the U_b boundary condition (10). These terms are important in cases considered here, in which $\mathrm{d}(\ell n\, a)/\mathrm{d}t$ may be of the same order as a. In contrast with Stahl and Warnatz,[4] we parameterize the flow with the unsteady strain rate parameter a, rather than with the tangential pressure curvature $1/x(\partial p/\partial x)$.[§] As argued in subsequent sections, this choice is more compatible with the modeling approach taken by flame embedding. As a result, we obtain the dynamic behavior of U_b given in Eq. (10).

Numerical Solution

Numerical solution of the governing equations is obtained via a fully implicit finite difference method, as necessitated by the stiffness of detailed kinetics. A first-order backward Euler formulation is used. In contrast to some previous formulations,[10] all of the governing equations are solved simultaneously, and thus the continuity equation (5) is in a sense an algebraic constraint on the implicit system.

In general, a first-order upwind discretization is applied to all convective terms, whereas diffusion terms are discretized to second-order accuracy using centered differences. Discretization of the continuity equation warrants special mention, however. Without an appropriate stencil, numerical oscillations in the mass flux profile are observed during translation of the flame with respect to the spatial grid; susceptibility to oscillations is high because the continuity equation is the only governing equation without physical dissipation. Thus, an upwind discretization is used. The term "upwind" is written with some qualification, because the continuity equation is not properly a transport equation and $\partial V/\partial y$ is not a convective term per se. Nonetheless, taking the positive sign outside $\partial V/\partial y$ to suggest a positive upwind velocity, the following discretization of the continuity equation adds dissipation of the appropriate sign:

$$\frac{\partial \rho}{\partial t} + \frac{\partial V}{\partial y} + \rho U a = 0 \rightsquigarrow \frac{\rho_j^{n+1} - \rho_j^n}{\Delta t} + \frac{V_j^{n+1} - V_{j-1}^{n+1}}{y_j - y_{j-1}} + \rho_j^{n+1} U_j^{n+1} a^{n+1} = 0 \tag{12}$$

This discretization of $\partial V/\partial y$ prevents direct implementation of a stagnation-point boundary condition. Instead, a boundary value on the mass flux V must be chosen at $y=-\infty$. The boundary value is arbitrary provided that it is large enough for the flame to stabilize at a lower mass flux because V decreases in the direction of the stagnation point. If the boundary value is too large, on the other hand, the flame (or for that matter, the stagnation point) may not fall within the computational domain. The boundary value can thus be set to any reasonable number based on the size of the computational domain and the strain rate. The solution to the problem matches the mass flux profile to the flame location, as reflected in the profiles of T, Y_k, ρ, and U.

In computations with unsteady strain rate, this boundary condition on V must be updated intermittently. The strain rate parameter a can easily vary one or two orders of magnitude in a given computation; such a change in strain rate, with a fixed boundary value on the mass flux through the flame, causes the flame to translate rapidly with respect to the grid. As the flame nears the boundary of the computational domain, successive regriddings become necessary. This scenario is not only cumbersome, but computationally taxing. To avoid this situation while retaining the boundary condition $V(y=-\infty)$, we implement a method to update the mass flux profile in the case of unsteady strain rate. At the start of time step $n+1$, an initial guess for V^{n+1} is obtained by integrating the continuity equation with a^{n+1}, U^n, and ρ^n:

$$\frac{\rho_j^n - \rho_j^{n-1}}{\Delta t} + \frac{V_j^{n+1,\mathrm{guess}} - V_{j-1}^{n+1,\mathrm{guess}}}{y_j - y_{j-1}} + \rho_j^n U_j^n a^{n+1} = 0 \tag{13}$$

In one step, this expression updates the boundary value on V at $y=-\infty$ and generates a new guess for V^{n+1}. Updating the boundary value on V thus minimizes flame translation for fast convergence.

All of the spatial discretizations are performed on a nonuniform adaptive grid, permitting a dynamic clustering of grid points in regions where spatial gradients are strong and, thus, ensuring adequate resolution through the reaction-diffusion zone over all of the integration time. The following criteria for grid refinement, similar to those employed in Sandia's PREMIX code[33] were enforced at each time step. First, the gradient of each scalar must be adequately resolved, relative to its range:

$$\frac{\alpha}{x}\left|\max_j \varphi - \min_j \varphi\right| < |\varphi_{j+1} - \varphi_j| < \alpha\left|\max_j \varphi - \min_j \varphi\right| \tag{14}$$

Here φ is chosen to include all of the dependent variables, T, Y_k, U, and V, as well as each chemical source term $\dot{w}_k$; α is a tolerance parameter on the order of 0.1, and the point-removal parameter κ is typically chosen around 5. Second derivatives are subject to an

[§] As pointed out by Stahl and Warnatz,[4] these quantities are related by the following ODE, which follows from Eq. (1):

$$\frac{1}{x}\frac{\partial p}{\partial x} = -\rho_u\left(a^2 + \frac{\mathrm{d}a}{\mathrm{d}t}\right)$$

analogous criterion:

$$\frac{\beta}{\kappa}\left|\max_j\left(\frac{\partial\varphi}{\partial y}\right)-\min_j\left(\frac{\partial\varphi}{\partial y}\right)\right|<\left|\left(\frac{\partial\varphi}{\partial y}\right)_{j+1}-\left(\frac{\partial\varphi}{\partial y}\right)_j\right|$$

$$<\beta\left|\max_j\left(\frac{\partial\varphi}{\partial y}\right)-\min_j\left(\frac{\partial\varphi}{\partial y}\right)\right| \tag{15}$$

The final criterion forces the grid to be relatively uniform:

$$\gamma<\frac{y_{j+1}-y_j}{y_j-y_{j-1}}<\frac{1}{\gamma} \tag{16}$$

A grid point is removed when it simultaneously violates the three lower inequalities in Eqs. (14–16). Linear interpolation is used to calculate the value of the dependent variables at any new grid point.

The time step for integration is constant, typically chosen on the order of 1 μs. A time convergence study and a detailed grid resolution study are presented in the next section. At each time step, discretization reduces the governing partial differential equations to a set of nonlinear algebraic equations. The nonlinear system can be written as

$$\boldsymbol{F}(\boldsymbol{x})=\boldsymbol{0}, \qquad \boldsymbol{F}:\mathbb{R}^n\to\mathbb{R}^n \tag{17}$$

The output of the function $\boldsymbol{F}$ is a vector containing residuals of the discretized governing equations, whereas $\boldsymbol{x}$ is the solution vector, containing profiles of each fundamental variable, Y_k, T, U, and V.

We implement a set of numerical methods to solve Eq. (17) efficiently and robustly.[25] An inexact Newton iteration (see Ref. 34) converges to the solution of the nonlinear equations but avoids precisely solving the Newton condition far away from a solution, when the linear model of Newton's method may be poor. In other words, each Newton step $\boldsymbol{s}_i$ is found via the following expression:

$$\|\boldsymbol{F}(\boldsymbol{x}_i)+\boldsymbol{F}'(\boldsymbol{x}_i)\boldsymbol{s}_i\|\le\eta_i\|\boldsymbol{F}(\boldsymbol{x}_i)\| \tag{18}$$

The key parameter in inequality (18) is $\eta_i\in[0,1)$, the forcing term. The inexact Newton condition essentially restates the exact Newton condition from the perspective of an iterative linear solver. An iterative method is used to find an approximate solution to the exact Newton condition, $\boldsymbol{F}'(\boldsymbol{x}_i)\boldsymbol{s}_i=-\boldsymbol{F}(\boldsymbol{x}_i)$, and η_i specifies the tolerance to which this solution $\boldsymbol{s}_i$ is found.

Proper specification of η_i can vastly enhance efficiency and convergence of the nonlinear solver. Far away from a solution, where the linear model may poorly describe the nonlinear surface of the function $\boldsymbol{F}$, it makes little sense to calculate each Newton step exactly. Doing so is computationally expensive and may result in little or no progress toward a solution; indeed, a less accurate solution of the Newton conditions may be more effective in reducing $\|\boldsymbol{F}\|$. The forcing term is thus chosen close to 1. If the linear model becomes accurate, however, a precise Newton step is likely to provide fast reduction in $\|\boldsymbol{F}\|$; the forcing term is thus chosen close to zero.

In our implementation, the inexact Newton method is coupled with a safeguarded backtracking globalization to improve its domain of convergence.[35] If the step $\boldsymbol{s}_i$ of the inexact Newton condition does not sufficiently reduce $\|\boldsymbol{F}\|$, the step is reduced by a scalar factor θ, essentially backtracking along the search direction. Backtracking continues until the condition on $\|\boldsymbol{F}\|$ is met because, in a sufficiently small neighborhood of the trial solution $\boldsymbol{x}_i$, the linear model must indicate the correct downward path; the Newton equation is consistent.

Solution of the linear system at each Newton iteration proceeds via a Krylov subspace method Bi-Conjugate Gradient Stabilized (BiCGSTAB).[36] Like all Krylov subspace methods, BiCGSTAB is based on the idea of projecting a problem onto a lower-dimensional Krylov subspace, making it particularly desirable for large-scale systems. Because detailed chemistry renders our linear system ill-conditioned, BiCGSTAB must be accelerated with an incomplete lower–upper (LU) factorization preconditioner; here, we implement ILUTP, a refinement of ILU preconditioning developed by Saad.[37] ILUTP provides an LU-factorization of the Jacobian matrix $\boldsymbol{F}'$ but regulates fill in of L and U based on a threshold parameter; it also provides for pivoting, in which $\boldsymbol{F}'$ is permuted to ensure diagonal dominance. The result is a preconditioned system with a smaller and more uniformly distributed eigenvalue spectrum.

Numerical Validation

Grid Resolution

Before employing the elemental flame model in studies of the flame embedding approach, we validate the numerical treatment and underlying formulation. We begin by presenting a grid-resolution study, shown in Fig. 1. The structure of a steady-state, planar premixed methane–air flame is computed for four cases of the grid parameters defined in Eqs. (14–16). The reactants mixture is stoichiometric, and the products mixture is in equilibrium at the adiabatic flame temperature, with an additional 20% N_2 by volume present in both the reactants and products streams. The thermodynamic pressure is 1 atm, and the strain rate parameter a is constant at 120 s^{-1}. The grid-resolution parameters α and β are varied over one order of magnitude, from $\alpha=0.2$ and $\beta=0.8$ (the least-resolved case) to $\alpha=0.02$ and $\beta=0.08$ (the most-resolved case). The grid-uniformity parameter γ defined in Eq. (16) is held constant at $\gamma=2.5$. The computational domain is 4.0 cm in length. As seen in Fig. 1, the computed profiles of temperature, selected species, and heat release rate ($\dot{w}_T$, i.e., the source term in the energy equation) match very closely for all four cases, so closely as to be relatively indistinguishable over much of the flame structure. The solution to the least-resolved case contained 121 grid points and a minimum grid spacing of 14.6 μm, whereas the most resolved case used 453 grid points and a minimum grid spacing of 2.1 μm.

The grid independence observed in this study indicates that profiles of the solution variables Y_k, T, U, and V and of the corresponding convection, diffusion, and production terms in the governing equations are well resolved by the adaptive grid for the chosen discretizations. For the remainder of the elemental flame calculations presented in this paper, we fix $\alpha=0.1$ and $\beta=0.4$.

Time Resolution

We examine the time step resolution of the numerical formulation by computing the response of a premixed methane–air flame to an imposed transient in the strain rate parameter $a(t)$. The initial condition is the same steady-state, diluted stoichiometric flame used in the grid-resolution study. The strain rate parameter $a(t)$ is increased linearly from 120 to 1000 s^{-1} over the course of 2 ms, then held constant at 1000 s^{-1} for another 3 ms; mixture boundary conditions match those of the initial condition and are held constant throughout. The flame response is characterized by the integrated heat release rate $\dot{Q}(t)$, which is plotted vs time for four different values of the time step in Fig. 2. The time steps range over approximately 1.5 orders of magnitude, from 10 to 0.5 μs. As seen in Fig. 2, the calculated heat release rate histories match very closely, suggesting that the internal timescales governing the flame response are well resolved.

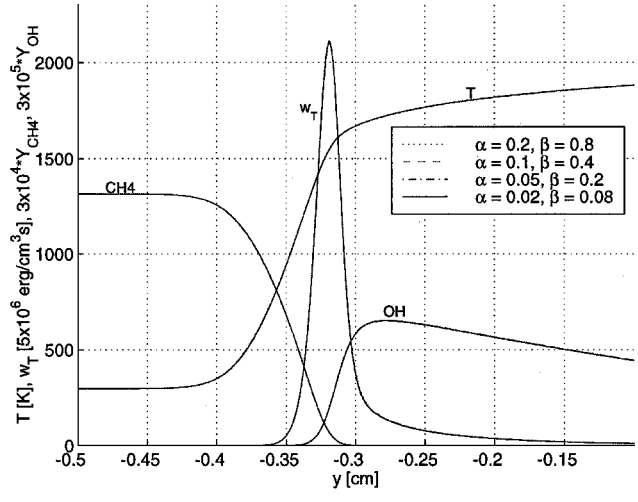

Fig. 1 Structure of a stoichiometric premixed methane–air flame, $a=120\ s^{-1}$, for various values of the grid-refinement parameters α and β defined in Eqs. (14) and (15).

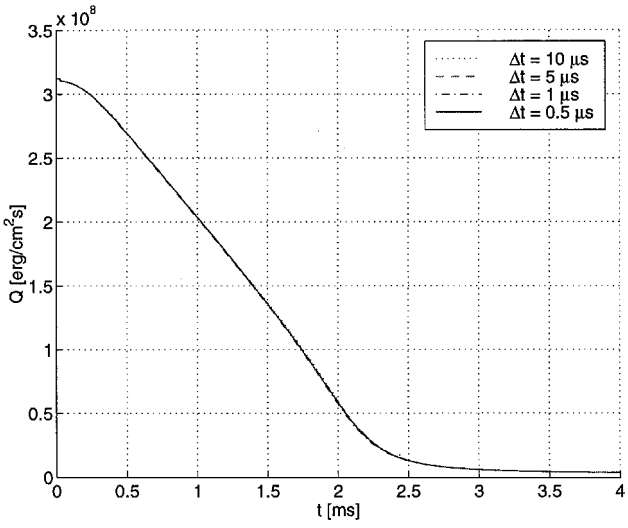

Fig. 2 Integrated heat-release rate history $\dot{Q}(t)$ resulting from a 2-ms linear rise in strain rate $a(t)$ from 120 to 1000 s^{-1}, computed with various values of Δt.

Note that Fig. 2 clearly shows that the flame response is unsteady. The imposed strain rate transient lasts only 2 ms, yet the heat release rate takes an additional 1.5 ms to reach its equilibrium value, at which point the flame is essentially quenched.[16] Also, we mention that the speed and range of the strain rate parameter transient selected for this study is typical of the transients observed in the flame–vortex interactions to be presented in the next section. For the remainder of the elemental flame calculations presented, we take $\Delta t = 1.0\ \mu$s.

Results

We examine the validity of the flame embedding approach via comparison with numerical simulations of two-dimensional flame–vortex interactions, as depicted in Figs. 3 and 4. Figures 3 and 4 show successive snapshots of a counter-rotating vortex pair moving toward a freely propagating premixed flame. Because the domain is symmetric, only the left half of the interaction is shown. A grayscale indicates temperature, and contour lines depict vorticity. In all cases, the vorticity field contorts and strains the flame surface; thus, the simulations capture the impact of transient strain rate and curvature on the flame's internal structure and heat release rate.

Simulations of Flame–Vortex Interaction

Four cases of flame–vortex interaction were computed, corresponding to a two-by-two "matrix" of vortex strengths and length scales whose parameters are given in Table 1. The initial circulation Γ, the vortex characteristic dimension δ (taken as the initial Gaussian vortex width), and the initial center-to-center separation of the vortex pair δ_{cc} are varied to control the induced flowfield. For brevity, we include two-dimensional snapshots for only two cases. Figures 3 and 4 correspond to cases 1 and 4, respectively.

A detailed description of the model formulation and the numerical scheme used in our simulations of flame–vortex interaction may be found elsewhere.[38–40] Governing equations are developed in two dimensions using, as with the elemental flame model, the low-Mach-number approximation and assuming constant stagnation pressure. Thermal diffusion velocities are neglected. Spatial discretization is performed using second-order central differences on a uniform mesh with cell size $\Delta x = \Delta y = 15.6\ \mu$m, ensuring adequate representation of internal flame structure.[17,41] A stiff, operator-split second-order time integration scheme is used.[39,40] In the cases presented here, the computational domain measures 0.8 cm in the horizontal (x) direction and 4.0 cm in the vertical (y) direction. Symmetry boundary conditions are applied in the horizontal direction, and outflow boundary conditions are applied in the vertical direction.

The reactants mixture is stoichiometric methane–air at 298 K, diluted with an additional 20% N_2 by volume. The thermodynamic pressure is 1 atm; dilution lowers the adiabatic flame temperature to 1965 K, thus reducing the burning rate and lengthening the flame

Table 1 Flow parameters used in four cases of flame-vortex interaction: initial vortex circulation Γ, initial Gaussian vortex width δ, initial vortex pair separation δ_{cc}

Case	Γ, cm^2/s	δ, cm	δ_{cc}, cm
1	0.035	0.10	0.50
2	0.035	0.05	0.25
3	0.070	0.10	0.50
4	0.070	0.05	0.25

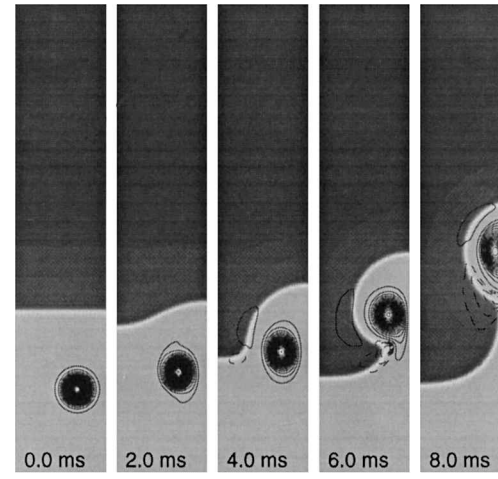

Fig. 3 Premixed flame interaction with a counter-rotating vortex pair, case 1. Vertical right-hand side of each frame is centerline of vortex pair; grayscale indicates gas temperature, with darker shading corresponding to burned combustion products; solid/dashed contours delineate levels of positive/negative vorticity.

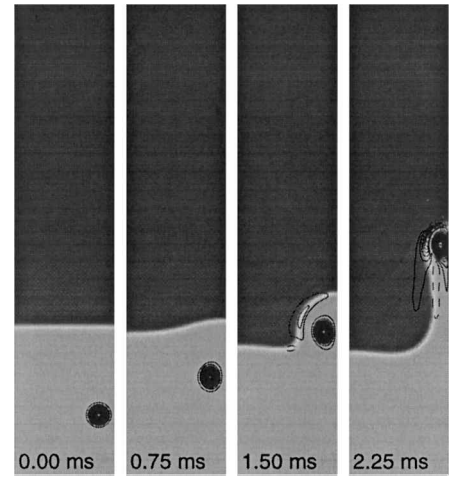

Fig. 4 Premixed flame interaction with a counter-rotating vortex pair, case 4; contour definitions analogous to Fig. 3.

timescale. The same C_1 mechanism[32] used in the preceding sections is applied here. For computational efficiency, however, N_2 is assumed dominant so that the diffusion velocity of any other species is approximated by binary diffusion into N_2 at the local temperature. Mixture transport properties μ and λ are set to those of N_2 at the local temperature. Subsequent calculations employing the elemental flame model also make use of this nitrogen-dominant transport scheme, rather than the mixture-averaged transport properties used in the original elemental flame formulation. Thus, simulations of two-dimensional flame–vortex interaction and flame embedding calculations are compared using identical transport and kinetics.

Initial conditions for simulation of flame–vortex interaction are constructed as follows: The velocity field (u, v) induced by a periodic row of Gaussian vortex pairs is superimposed on fields of temperature, density, and mass fraction, T, Y_k, and ρ, corresponding to an unstrained premixed flame, computed using PREMIX.[33]

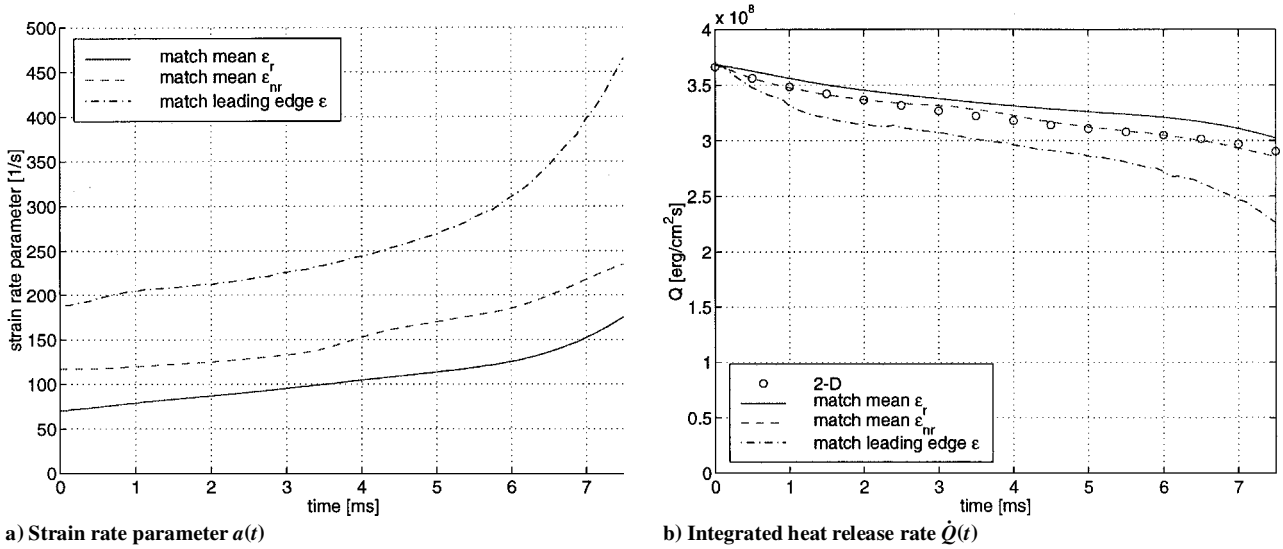

a) Strain rate parameter $a(t)$ **b) Integrated heat release rate $\dot{Q}(t)$**

Fig. 5 Case 1, strain rate parameter $a(t)$ derived from the centerline of the flame–vortex interaction and corresponding integrated heat release rate histories $\dot{Q}(t)$ of the embedded flame.

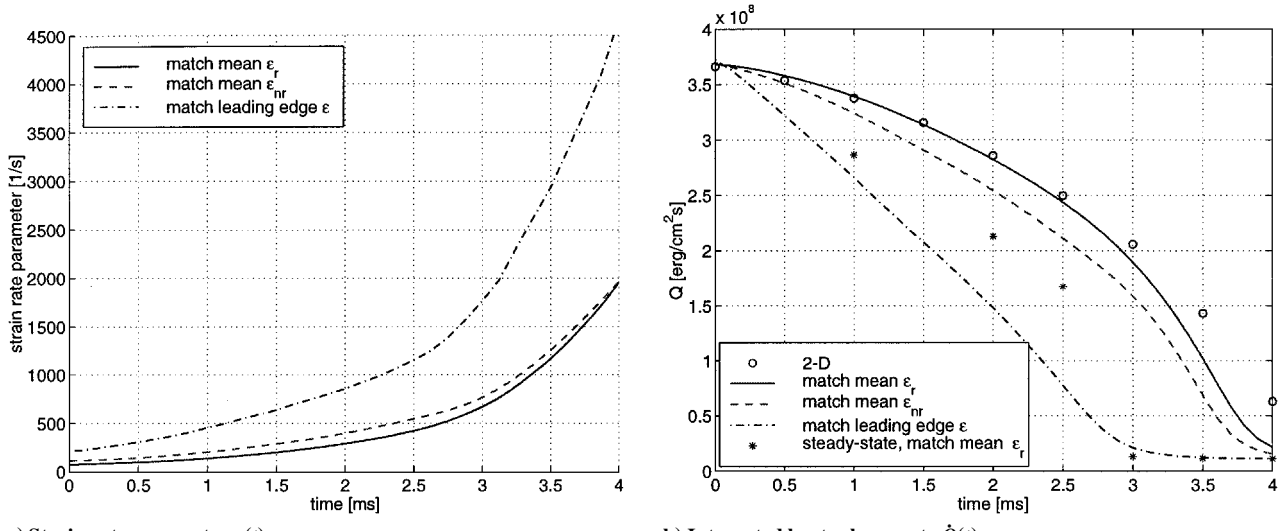

a) Strain rate parameter $a(t)$ **b) Integrated heat release rate $\dot{Q}(t)$**

Fig. 6 Case 2, strain rate parameter $a(t)$ derived from the centerline of the flame–vortex interaction and corresponding integrated heat release rate histories $\dot{Q}(t)$ of the embedded flame.

The flame surface is oriented horizontally, and so T, Y_k, and ρ are functions of y only. The flame is introduced at a distance where the impact of the vortex pair on the flame surface is negligibly small; the initial distance between the flame and the vortex pair is chosen so that the tangential strain rate at the 10% contour of Y_{CH_4} was 116.9 s^{-1} in all four cases.

Because some sections of the flame surface experience substantial curvature, an effect that has not yet been included in the elemental flame model, we focus on the relatively flat section of the flame surface intersecting the vortex pair centerline. A few general observations can be made about the impact of the flow on this flame element, as shown in Figs. 5a–8a: In cases 1 and 3, the strain rates at the intersection of the flame surface and the centerline are relatively low, $\mathcal{O}(300\ s^{-1})$, rising weakly due to the relatively large distance between the two vortices. In cases 2 and 4, where the vortex length scales are halved, the corresponding strain rates rise more sharply, finishing an order of magnitude higher. All cases show similar evolution of the flame surface topology, as seen in Figs. 3 and 4: an early stage, before the vortex pair penetrates the plane of the flat flame, characterized by relatively low and slowly rising strain rates, and a later stage, following intrusion of the vortex pair into a curving flame "mushroom," characterized by higher and more quickly rising strain rates. As the flow timescale (governed by δ_{cc} and Γ) is halved (e.g., from case 1 to case 3, or from case 2 to case 4), the time over which the flame surface topology undergoes this evolution drops accordingly.

As a testbed for validation of the flame embedding approach, we extract the Lagrangian history of flow conditions—in particular, the strain rate—local to the centerline flame element and use this history as an input to the elemental flame model. We then examine the ability of the elemental flame model to predict the transient heat release rate and flame structure of the two-dimensional flame element, that is, whether the unsteady flame–flow interaction described earlier can indeed be captured by a Lagrangian embedded flame. The quality of the comparison hinges on specifying the input strain rate parameter $a(t)$ of the elemental flame model. Clearly $a(t)$ should characterize the strain rate induced by the flow on the flame structure, but selecting where to evaluate this strain rate with respect to the flame surface in the two-dimensional simulation turns out to be a nontrivial task under certain flow conditions. This is in part because, as suggested by Figs. 3 and 4 and Table 1, the length scale of the vortices, $\mathcal{O}(1\ mm)$, may be of the same order of magnitude as the flame thickness, and thus the vortex-induced strain rate may vary significantly within the flame structure, making it difficult to find a representative, single value for the applied strain rate. We find this to be particularly true of cases 2 and 4. These ideas will be made more precise as we explore three different means of selecting a value for the strain rate parameter $a(t)$.

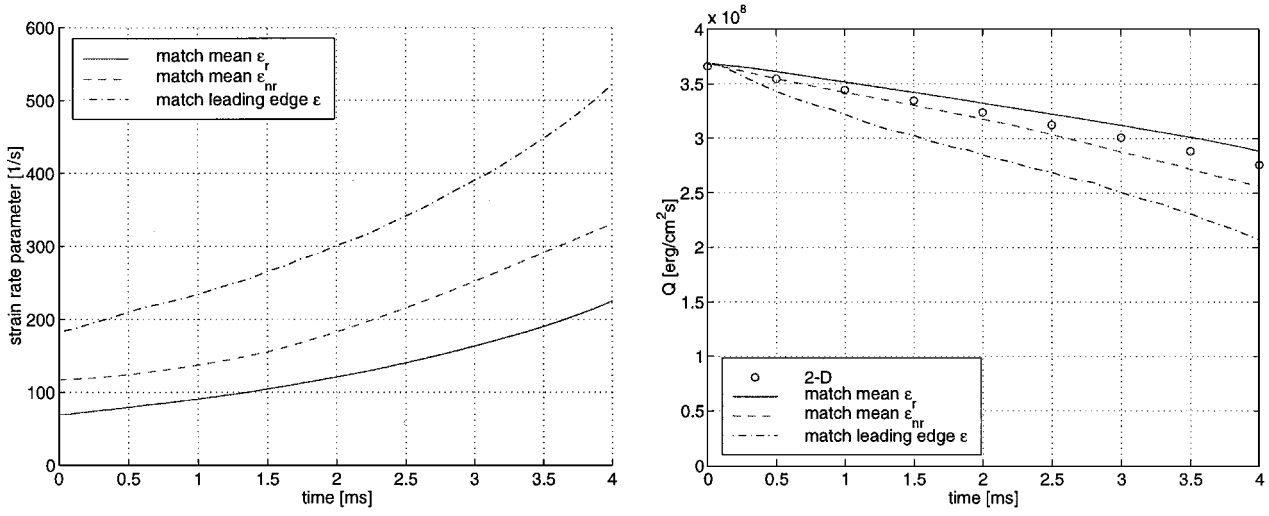

a) Strain rate parameter $a(t)$ **b) Integrated heat release rate $\dot{Q}(t)$**

Fig. 7 Case 3, strain rate parameter $a(t)$ derived from the centerline of the flame–vortex interaction and corresponding integrated heat release rate histories $\dot{Q}(t)$ of the embedded flame.

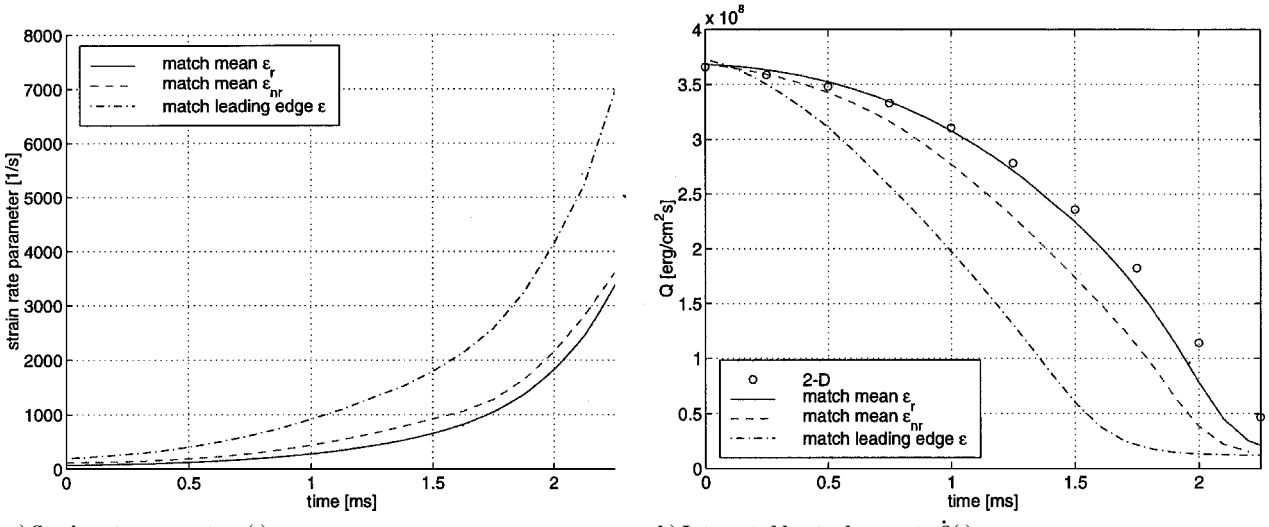

a) Strain rate parameter $a(t)$ **b) Integrated heat release rate $\dot{Q}(t)$**

Fig. 8 Case 4, strain rate parameter $a(t)$ derived from the centerline of the flame–vortex interaction and corresponding integrated heat release rate histories $\dot{Q}(t)$ of the embedded flame.

Matching Leading-Edge Strain Rates

By construction, the strain rate parameter $a(t)$ of the elemental flame model is equal to the strain rate measured at the cold side of the elemental flame.[¶] [Referring to Eq. (8), U is essentially constant and equal to 1 from the cold boundary to the leading edge of the flame.] Thus, a natural approach is to set $a(t)$ equal to the strain rate at the leading edge of the two-dimensional flame element. We proceed by extracting the strain rate tangential to a 99% contour of Y_{CH_4} from the centerline of each flame–vortex interaction. This contour is a reliable indicator of the flame leading edge. By symmetry, all scalar contours are normal to the centerline, and so the tangential strain rate $\boldsymbol{t}\cdot\boldsymbol{e}\cdot\boldsymbol{t}$ extracted here is just $\partial u/\partial x|_{x=x_{CL}}$, where $\boldsymbol{e}$ is the rate-of-strain tensor.

The leading-edge strain rate is plotted as a function of time in Figs. 5a–8a. For cases 2 and 4, the leading-edge strain rate rises 1.5 orders of magnitude over a time period smaller than the propagation timescale of the premixed flame ($\tau_f \equiv \Delta/S_u \approx 10$ ms, where Δ is a flame thickness). The burning of the centerline flame element is clearly not expected to respond quasi-steadily.

With an input strain rate parameter $a(t)$ in hand, the elemental flame requires only a starting condition and mixture boundary conditions matching those in the flame–vortex interaction. The mixture boundary conditions are constant in time, matching the nitrogen-diluted reactants and products mixtures of the flame–vortex interaction. Initialization is performed in a manner analogous to the initialization of the flame–vortex interaction simulations. At $t=0$, profiles of T, Y_k, and ρ are obtained from the same unstrained premixed flame solution and superimposed on profiles of U and V corresponding to $a(t=0)$. Integration then proceeds using $a(t)$.

For each case, the resulting integrated heat release rate $\dot{Q}$ is shown by a dash–dot line in Figs. 5b–8b. Circles represent the heat release rate of the two-dimensional flame element, computed by integrating $\dot{w}_T$ along the centerline coordinate of Figs. 3 and 4. The heat release rate falls with increasing strain rate in both flames, an expected trend, but the elemental flame clearly underpredicts the heat release rate at the two-dimensional flame surface. This discrepancy widens at higher strains and larger times and is more extreme in cases 2 and 4 than in cases 1 and 3. The elemental flame approaches extinction near $t=3.5$ ms in case 2 and $t=2.0$ ms in case 4, while the two-dimensional flame element continues to burn.

Underprediction of $\dot{Q}$ suggests that the strain rate throughout the elemental flame is too high in comparison to the strain rate through the two-dimensional flame surface. Suspicion of such a strain rate mismatch is confirmed in Fig. 9. Here, the thick solid line represents the tangential strain rate ($\epsilon^{(2d)} = \partial u/\partial x|_{x=x_{CL}}$) along the centerline of the flame–vortex interaction for case 1, at $t=6.5$ ms. The open

[¶]For clarity, we reserve the symbol a to denote the strain rate parameter of the elemental flame model; the symbol ϵ may denote any other strain rate. To refer specifically to strain rates in the flame–vortex simulations or in the elemental flame, we may use $\epsilon^{(2d)}$ and $\epsilon^{(1d)}$, respectively.

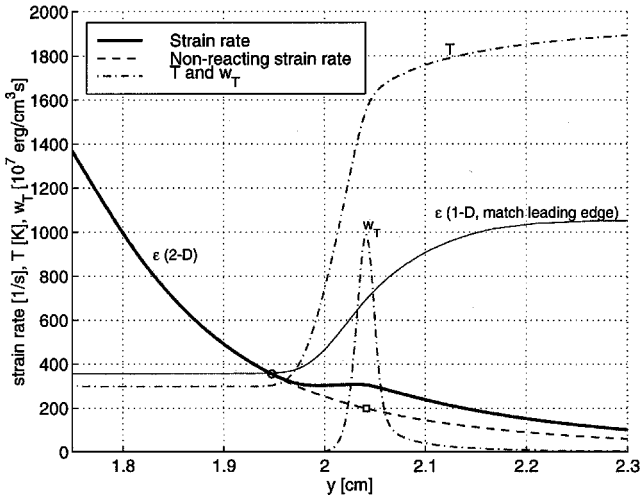

Fig. 9 Strain, rate profiles in the two-dimensional flame element, case 1, $t = 6.5$ ms: ——, actual strain rate; – – –, extrapolated nonreacting strain rate; ○, strain rate at leading edge of flame, where ϵ_r and ϵ_{nr} begin to diverge; □, mean nonreacting strain rate; and ——, strain rate profile in the corresponding elemental (one-dimensional) flame, matching the leading-edge strain rate.

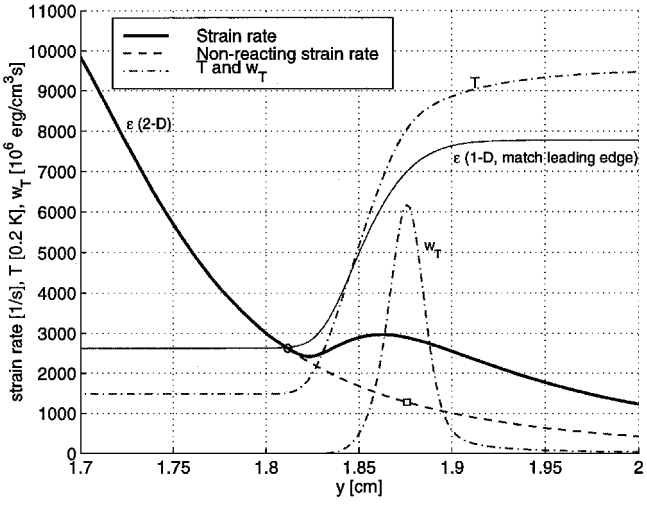

Fig. 10 Strain, rate profiles in the two-dimensional flame element, case 4, $t = 1.75$ ms: ——, actual strain rate; – – –, extrapolated nonreacting strain rate; ○, strain rate at leading edge of flame, where ϵ_r and ϵ_{nr} begin to diverge; □, mean nonreacting strain rate; and ——, strain rate profile in the corresponding elemental (one-dimensional) flame, matching the leading-edge strain rate.

circle indicates the location of and strain rate at the flame leading edge. The two-dimensional strain rate falls when moving across the flame from reactants to products, except for a small hump around the reaction zone (indicated by $\dot{w}_T$). In the same plot, the thin solid line shows the strain rate profile $\epsilon^{(1d)}$ in the elemental flame, also at $t = 6.5$ ms, with $a(t)$ chosen to match the leading-edge strain rate. This profile rises monotonically from a reactants-side value of a to a products-side value of aU_b. Clearly, the strain rate in the two-dimensional flame is significantly lower than that in the elemental flame. In Figs. 9 and 10 the elemental flame strain rate profile is placed so that the leading edges of the one- and two-dimensional flames coincide. Figure 10 shows analogous results for the more highly strained flow field of case 4, at $t = 1.75$ ms. Now the decrease in $\epsilon^{(2d)}$ ahead of the two-dimensional flame is even steeper, whereas the hump around the reaction zone is more pronounced. Nonetheless, the strain rate $\epsilon^{(1d)}$ in the elemental flame is still higher than $\epsilon^{(2d)}$ over the entire flame structure. In both cases, the two-dimensional strain rate profiles—and the average strain rate within each two-dimensional flame—differ markedly from those of the elemental flame.

The strain rate profile ahead the flame along the centerline of each flame–vortex interaction is typical of that induced by a counter-rotating vortex pair. Extrapolating this strain rate into the flame region, the dashed line in Figs. 9 and 10 represents the strain rate that would have existed in the absence of combustion, that is, the monotonically decreasing strain rate induced by the vortex pair. The dashed line can thus be considered the underlying or nonreacting strain rate through the flame, denoted by $\epsilon_{nr}^{(2d)}$. Volumetric expansion in the flame induces an additional flowfield, which modifies the underlying strain rate to produce the actual strain rate profile, shown by the thick solid line. A similar superposition is responsible for the strain rate profile in the elemental flame, but in that case, the underlying strain rate is constant and equal to a.

The procedure used to construct the dashed lines in Figs. 9 and 10, corresponding to $\epsilon_{nr}^{(2d)}$, is as follows: At a given time step, the velocity field of the vortex pair is approximated analytically as the velocity field induced by two counter-rotating Gaussian vortices. This velocity field is differentiated, yielding a model for the nonreacting strain rate at the centerline:

$$\epsilon_{nr}^{(2d)} = \left.\frac{\partial u}{\partial x}\right|_{x = x_{CL}} = \frac{2\Gamma}{\pi} x_0 (y - y_0)\left[\frac{1 - \exp(-r^2/\delta^2)}{r^4} - \frac{\exp(-r^2/\delta^2)}{r^2\delta^2}\right] \quad (19)$$

where $r^2 \equiv x_0^2 + (y - y_0)^2$. Here Γ is the strength of each vortex, δ is the size of the Gaussian vortex core, x_0 is the horizontal offset of each vortex from the centerline, and y_0 is height of the centerline of the vortex pair. These model parameters are computed at a given time step by fitting $\epsilon_{nr}^{(2d)}$ to the strain rate along the centerline of the two-dimensional simulation in regions ahead of the leading edge of the flame, where the strain rate is due entirely to the vortical flowfield. A nonlinear least-squares method is used for fitting.

The preceding results indicate that the vortex-induced strain rate $\epsilon_{nr}^{(2d)}$ may vary substantially within the flame structure, countering the assumption that the flame is thin with respect to length scales in the flow. Thus, using $\epsilon^{(2d)}$ at the flame leading edge as the value of the strain rate parameter a may be misleading because $\epsilon_{nr}^{(2d)}$ decays rapidly within the flame structure. Cases 2 and 4 of the flame–vortex interaction, in particular, may be on the boundary of the thin-flame regime. Indeed, if we construct a suitable nondimensionalization for the length scale of strain rate variation, $\mathcal{E} \equiv \Delta/\epsilon(\mathrm{d}\epsilon/\mathrm{d}y)$, where Δ is a flame thickness, we find that $\mathcal{E}$, computed just ahead of the flame leading edge, is $\mathcal{O}(1)$ for all four cases, although approximately three times larger for case 4 than for case 1.

Matching Averaged Nonreacting Strain Rates

In the face of generic variations through the flame structure of the strain rate imposed by the outer flow, we must find alternative approaches to extract representative values of a from the two-dimensional simulations. Rather than setting a equal to the leading-edge strain rate of the two-dimensional flame element, a should be matched to a strain rate that is averaged across the two-dimensional flame structure. To find this value, we use Eq. (19) to construct a model for the underlying nonreacting strain rate $\epsilon_{nr}^{(2d)}$ throughout the flame. Note that the simulations of flame–vortex interaction only yield strain rates represented by the thick solid lines in Figs. 9 and 10 and that $\epsilon_{nr}^{(2d)}$ represents an attempt to estimate the strain rate that would have been exerted in the absence of a flame.

With a model of $\epsilon_{nr}^{(2d)}(y)$ in hand, it can be extrapolated through the flame region. The "averaged" nonreacting strain rate $\bar{\epsilon}_{nr}^{(2d)}$ is simply taken to be $\epsilon_{nr}^{(2d)}$ at the heat release rate maximum, that is, in the center of the reaction zone, as marked with a square in Figs. 9 and 10. We then put $a(t) = \bar{\epsilon}_{nr}^{(2d)}$ and obtain an input strain rate history, shown for each case by the dashed line in Figs. 5a–8a. Figures 5a–8a show that this value of $a(t)$ is on the whole much smaller than the leading-edge strain rate.

Integrated heat release rates thus obtained are shown by dashed lines in Figs. 5b–8b. In general, this scheme shows marked improvement over the matching of leading-edge strain rates explored in the preceding section. Agreement with the two-dimensional heat release rate is quite good over the entire interactions of cases 1 and 3. Agreement is also close for much of cases 2 and 4, diverging at higher strain rates and long time. Divergence may be due in large

part to the approximations used to calculate $\epsilon_{\mathrm{nr}}^{(2\mathrm{d})}$. As it approaches the flame surface, the vortex pair is distorted significantly due to volumetric expansion and baroclinic vorticity generated across the flame, and thus, the Gaussian vortex approximation may become poor. Inaccuracy in the model used to predict $\epsilon_{\mathrm{nr}}^{(2\mathrm{d})}$ does not negate the principle of matching the mean nonreacting strains, however. Indeed, in some cases of direct flame embedding simulation, the exact value of $\epsilon_{\mathrm{nr}}^{(2\mathrm{d})}$ is available from the outer flow solution, regardless of the complexity of the vorticity field.[26,28]

Matching Averaged Reacting Strain Rates

A third approach for evaluating the strain rate parameter $a(t)$ in the embedded flame is to match the mean reacting strain rate in the two-dimensional flame to the mean reacting strain rate in the elemental flame. In both cases, by reacting strain rate, we simply mean the strain rate in the presence of the flame. We obtain the mean reacting strain rate from the flame–vortex interactions by computing the arithmetic mean of strain rates tangential to leading and trailing contours of the flame surface: the 99% contour of $Y_{\mathrm{CH_4}}$ and the 90% contour of $Y_{\mathrm{CO_2}}$. The resulting value is denoted by $\bar{\epsilon}_r^{(2\mathrm{d})}$. A mean reacting strain rate in the elemental flame can be defined similarly: Because the strain rate $\epsilon^{(1\mathrm{d})}$ rises from a value of a on the reactants side to aU_b on the products side, we have $\bar{\epsilon}_r^{(1\mathrm{d})} \equiv a[1 + U_b(t)]/2$. Now we set $\bar{\epsilon}_r^{(1\mathrm{d})} = \bar{\epsilon}_r^{(2\mathrm{d})}$ and use this condition to compute $a(t)$. The resulting expression and ODE, derived from the definition of $\bar{\epsilon}_r^{(1\mathrm{d})}$ and Eq. (10), are as follows:

$$a(t) = 2\bar{\epsilon}_r^{(2\mathrm{d})} \Big/ (1 + U_b) \tag{20}$$

where

$$\frac{\partial U_b}{\partial t} = -\frac{\rho_b}{\rho_u + \rho_b}\left(2U_b^2\bar{\epsilon}_r^{(2\mathrm{d})} + U_b(1+U_b)\frac{1}{\bar{\epsilon}_r^{(2\mathrm{d})}}\frac{\partial \bar{\epsilon}_r^{(2\mathrm{d})}}{\partial t}\right) + \frac{\rho_u}{\rho_u + \rho_b}\left(2\bar{\epsilon}_r^{(2\mathrm{d})} + (1+U_b)\frac{1}{\bar{\epsilon}_r^{(2\mathrm{d})}}\frac{\partial \bar{\epsilon}_r^{(2\mathrm{d})}}{\partial t}\right) \tag{21}$$

In effect, this scheme matches the strain rate in the reaction zone of the elemental flame with the strain rate in the reaction zone of the two-dimensional flame element, integrating the momentum equation across the elemental flame and computing the correct strain rate parameter $a(t)$ to achieve this matching. Strain rate parameter histories obtained in this fashion are shown by the solid lines in Figs. 5a–8a.

Heat release rates obtained with this approach are shown by the solid lines in Figs. 5b–8b. Agreement with the two-dimensional results is quite good in all four cases. In particular, predictions in cases 2 and 4 show improvement over the preceding scheme of matching the average nonreacting strain rates. The elemental flame heat release rates diverge from the two-dimensional values again only at long times, under conditions of extremely strong vortex-induced strain rates.

It is significant that overall good agreement is achieved in all four cases, particularly in cases 2 and 4, where, as mentioned earlier, the spatial variation of the vortex-induced strain rate is substantial over the flame thickness. This is important because these flames are not "thin" with respect to flow length scales (i.e., the thin-flame assumption is not strictly satisfied), yet a one-dimensional combustion zone model is still able to predict accurately the transient heat release rate resulting from the flame–vortex interaction.

We should make a remark here regarding the implementation of the second and third schemes in the context of flame embedding. To apply the second scheme, the strain rate variation ahead of the flame front, along a local normal to the flame, is obtained, extrapolated a flame thickness, and then used to specify $a(t)$ in Eqs. (2–5). In the third scheme, the values of the strain rate immediately ahead of and immediately behind the flame, that is, on the reactants side and the products side, should be averaged at each time step and used, in conjunction with Eqs. (20) and (21), to evaluate $a(t)$ before integration of Eqs. (2–5).

Results show that predictions using the elemental flame model are less dependent on the particular scheme chosen to estimate $a(t)$ in

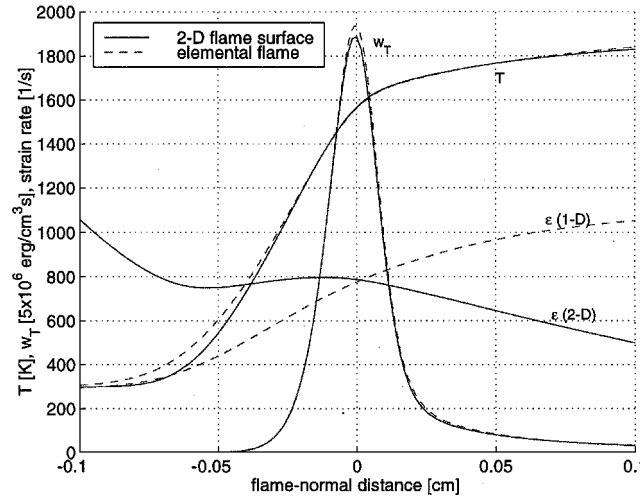

Fig. 11 Structure comparison between the one- and two-dimensional flame elements, case 2, $t = 2.0$ ms, showing T, heat release rate $\dot{w}_T$, and strain rate; both elements are at the same mean reacting strain.

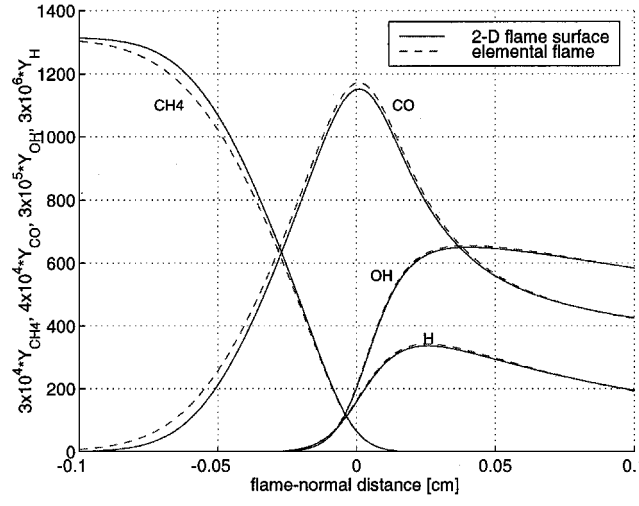

Fig. 12 Structure comparison between the one- and two-dimensional flame elements, case 4, $t = 1.0$ ms, showing various major and minor species; both elements are at the same mean reacting strain.

cases of weaker, more slowly varying strain rate (e.g., cases 1 and 3) than in cases of stronger, more sharply varying strain rate (e.g., cases 2 and 4). This is in part because the length scale of variation of the underlying vortex-induced strain rate is smaller in the latter cases, and thus, use of a spatial-averaging scheme to characterize $a(t)$ is more crucial. Another contribution to the observed trend is the weaker dependence of the heat release rate on the strain rate at low values of the latter.

Figure 11 compares the instantaneous structure of the elemental flame with that of the two-dimensional centerline flame element, for case 2 at $t = 2.0$ ms. The elemental flame calculation is one in which $a(t)$ was chosen to ensure matching of mean reacting strain rates. This comparison highlights the challenge inherent in using the elemental flame to predict the two-dimensional flame–vortex interaction. Though the mean strain rates in the two flames are equal, the strain rate distributions are qualitatively different, with ϵ falling through a plateau in the two-dimensional flame but rising monotonically in the one-dimensional flame, as discussed earlier. Although this disagreement may cause the remaining profiles to differ slightly, the elemental flame model is able to characterize the heat release rate in the two-dimensional reacting flow with good accuracy. A further comparison of elemental flame structure with that of the two-dimensional centerline flame is seen in Fig. 12; here, selected major species and radicals are shown for case 4 at $t = 1.0$ ms, again matching the mean reacting strain rates. The strain rate, temperature, and heat release profiles are qualitatively similar

to those in Fig. 11 and, thus, are not shown. The species profiles match well, with slight differences visible mostly in the preheat zone of the flame.

Note that the curvature of the flame surface at the centerline, always convex to the products side, provides a negative contribution to the overall flame stretch in all four interactions. Curvature is neglected in the current elemental flame model, and thus, this effect, although small for the centerline element in the flame–vortex interactions presented, may contribute to the discrepancies noted at long times, particularly for the smaller vortices of cases 2 and 4.

Results of steady-state simulations using the elemental flame model at selected values of the strain rate are included in Fig. 6b to illustrate the unsteady response of burning to the rapid changes in imposed strain rate. These points are the steady-state values of the heat release rate at averaged reacting strain rates equal to the instantaneous $\tilde{\epsilon}_r^{2d}$ extracted from the two-dimensional simulation. Clearly, even though the strain rate imposed on a flame can be changed arbitrarily by appropriate forcing of the surrounding flowfield, the response of the flame itself is dependent on its internal timescales. Thus, a flame can survive under transient strain rates that exceed its steady-state extinction strain rate, as long as the transients are sufficiently fast.[6,42,43] This phenomenon has been observed in earlier two-dimensional flame–vortex studies[16,17] and is apparent in the two-dimensional results shown here, where the steady-state extinction strain rate is approximately 700 s^{-1}. For $t \geq 3.0$ ms in case 2, burning persists under the dynamically applied strain, whereas at steady-state the flame would have undergone quenching. With the mean strain rate (reacting or nonreacting) as an input determining $a(t)$, the elemental flame model captures this important unsteady effect.

Conclusions

The flame embedding approach for turbulent combustion simulation seeks to model a wrinkled flame surface with an ensemble of one-dimensional elemental flames, each capturing the local impact of unsteady flow–flame interaction. This paper develops an elemental flame model incorporating detailed chemical kinetics and transport, parameterized by an unsteady strain rate and allowing arbitrary time dependence of mixture conditions. Unsteady features of the governing equations are developed and contrasted with previous unsteady strained flame studies. A numerical solution based on a globalized inexact Newton method and a preconditioned Krylov subspace linear solver is implemented to address the stiffness of detailed chemistry and ensure efficient, robust convergence. Grid- and time-resolution studies are presented to verify the accuracy of the code. Further verification is obtained by comparing the structure of a steady-state flame computed with the elemental flame formulation to that computed by OPPDIF (Appendix).

The concept of flame embedding is then explored in the context of two-dimensional flame vortex interactions. Detailed numerical simulations of flame–vortex interaction are performed for a matrix of vortex length scales and timescales. An element of the flame surface at the centerline of each interaction is selected for comparison with the flame embedding approach; the Lagrangian history of flow conditions local to the two-dimensional flame element is used to construct an input to the elemental flame model. Three different schemes for estimating the strain rate parameter $a(t)$ of the elemental flame model are developed. The first scheme matches the strain rate at the leading edge of the elemental flame with that of the two-dimensional flame element; the second and third schemes match the mean nonreacting strain rate and the mean reacting strain rate, respectively, of the two flames at each time step. We find that as the length scales of the vortices, in particular, the length scale of strain rate variation induced by the vortices, becomes comparable to the flame thickness, spatial averaging is necessary to determine $a(t)$, and thus the latter two schemes are more successful. The transient response of the heat release rate in the two-dimensional flame element is well predicted by the elemental flame, even in those cases when the length scale of strain rate variation induced by the vortices is small with respect to the flame thickness. A comparison of flame structures shows that the strain rate averaging schemes are able to match strain rates instantaneously near the reaction zone. These results suggest that the elemental flame may be used to accurately predict burning even when the flame is not thin with respect to flow structures.

Appendix: Steady-State Comparison with OPPDIF Solution

As an additional validation of the elemental flame model, we compared the structure of a steady-state flame computed with the elemental flame code to the structure of an identical flame computed using OPPDIF.[44] OPPDIF is a well-benchmarked steady-state strained flame code, employing the "two-parameter" formulation of the opposed-flow flame problem introduced by Kee et al.[45]

The two-parameter formulation poses the strained flame problem on a finite domain of length L, where L may be construed as the separation between two opposing nozzles. A similarity assumption reduces the governing equations to one dimension, in a coordinate normal to the flame. Arbitrary conditions may be specified for the axial velocity v and for the radial velocity divergence $(\partial u/\partial r)_{r=0}$ at each boundary. The radial pressure curvature $1/r(\partial p/\partial r)$ in the momentum equation is not an independent parameter; rather, it is an eigenvalue of the solution. The elemental flame, on the other hand, is a case of the "one-parameter" formulation, in which a single parameter, for example, the strain rate parameter a or the radial pressure curvature $1/r(\partial p/\partial r)$, characterizes the imposed flow. As detailed in the "Model Formulation" section, the one-parameter formulation assumes an infinite domain, taking the outer flow to be a stagnation-point potential flow (Hiemenz flow).

The two-parameter formulation was introduced in part for greater accuracy and flexibility in modeling laboratory experiments in which flames are stabilized in opposed-flow burners.[45] For the purposes of flame embedding, however, we find it more intuitive to parameterize our flame solution in terms of a flow-imposed strain rate, rather than in terms of finite domain boundary conditions, and thus we retain a one-parameter (unsteady) formulation.

Whereas it is not our purpose to present a detailed discussion contrasting one- and two-parameter strained flame formulations (the reader is instead referred to thorough discussions by Kee et al,[45] Stahl and Warnatz,[4] and Dixon-Lewis[46]), we simply note that a one-parameter strained flame solution may in principle be recovered from a two-parameter code such as OPPDIF by increasing the domain size and introducing the appropriate radial velocity divergence at each nozzle. Following Eqs. (8) and (11), the radial velocity divergence $(\partial u/\partial r)_{r=0}$ on the unburned side of the flame should be chosen equal to the strain rate parameter a, whereas on the burned side of the (steady-state) flame, it should be chosen as $a(\rho_u/\rho_b)^{1/2}$.

We pursue this approach in comparing an elemental flame solution with an OPPDIF solution. Both codes are used to compute the structure of an axisymmetric premixed methane–air flame, stoichiometric but with an additional 20% N_2 by volume present in both the reactants and products streams. The thermodynamic pressure is 1 atm. The codes are linked to the same 46-reaction C_1 kinetic model referenced earlier, as well as to identical transport models; mixture-averaged diffusion coefficients are computed with Sandia's TRANSPORT, and thermal diffusion velocities are neglected.

A steady-state elemental flame solution is obtained for an axisymmetric flame with the strain rate parameter a equal to 60 s^{-1}. Values of v and $(\partial u/\partial r)_{r=0}$ at the boundaries of the domain are then used to obtain an OPPDIF solution on a domain of exactly the same size as that of the elemental flame solution. According to Eq. (1), the OPPDIF-computed radial pressure curvature eigenvalue, $J = 1/r(\partial p/\partial r)$, should then be equal to $-\rho_u a^2$, where a is the strain rate parameter of the elemental flame solution. In practice, we find that $J \to -\rho_u a^2$ as the domain size $L \to \infty$ and that fairly large domain sizes are necessary to obtain close agreement. Here we present solutions for $L = 21.0$ cm. On this domain, the relative error between J and $-\rho_u a^2$ was 0.15%.

Temperature and selected species profiles for the OPPDIF solution and the elemental flame solution are shown together in Fig. A1. Very close agreement is observed in profiles of temperature, CH_4, H, and OH. In particular, the height and location of the H and OH peaks in the two solutions are relatively indistinguishable. A slight

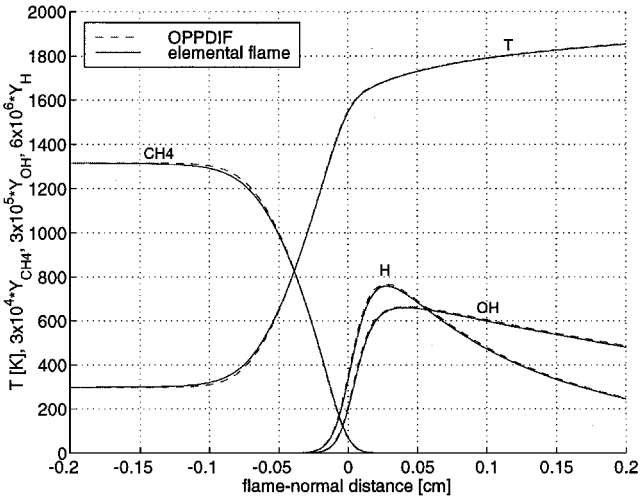

Fig. A1 Flame structure comparison, elemental flame vs OPPDIF.

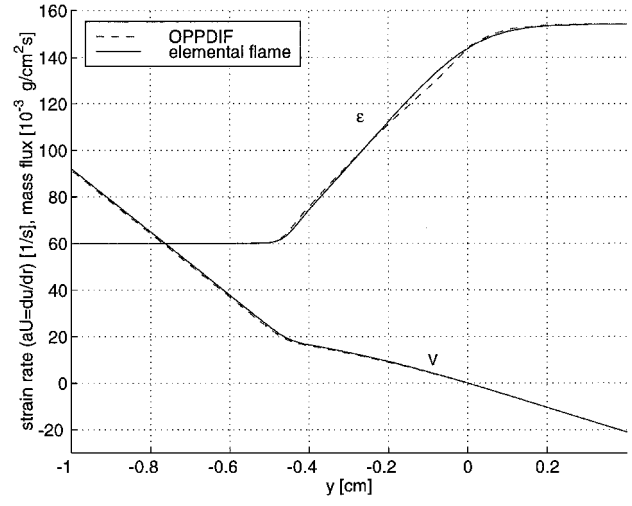

Fig. A2 Strain rate and mass flux profiles, elemental flame vs OPPDIF.

difference is noted in the shape of the temperature and CH_4 profiles near the flame's leading edge, but the overall matching of profile shapes and locations is quite close. Figure A2 shows profiles of mass flux through the flame, V, and strain rate ϵ, where the origin of the centerline coordinate y is taken to be the stagnation point in both solutions. Again, very close agreement is observed. The rise in strain rate through the elemental flame is slightly steeper than in the OPPDIF solution. As a result, the mass flux profiles diverge very subtly in the region immediately to the left of the the stagnation point because the slope of V is proportional to ϵ. It is not immediately clear why the shapes of the strain rate profiles differ in the flame region, other than differences in the primitive solution variables and their discretization on the underlying nonuniform grids. We do find, however, that the strain rate profile in the OPPDIF solution is somewhat dependent on the domain size L, whereas the strain rate profile in the elemental flame solution is quite insensitive to L. Nonetheless, the discrepancies observed are extremely small, and the computed flame structures match quite closely.

Acknowledgments

This work was supported by the U.S. Department of Energy, Basic Energy Sciences, MICS, under Contract DE-F602-98ER25355, by the BES Division of Chemical Sciences, Geosciences, and Biosciences, and through the Air Force Office of Scientific Research FRI Project F49620-95-C-0089. Y. M. Marzouk also acknowledges graduate fellowship support from the Fannie and John Hertz Foundation.

References

[1]Peters, N., "Length Scales in Laminar and Turbulent Flames," *Numerical Approaches to Combustion Modeling*, edited by E. S. Oran and J. P. Boris, AIAA, Washington, DC, 1991, Chap. 6, pp. 155–182.

[2]Peters, N., "Laminar Flamelet Concepts in Turbulent Combustion," *Proceedings of the Combustion Institute*, Vol. 21, 1986, pp. 1231–1250.

[3]Bray, K. N. C., and Peters, N., "Laminar Flamelets in Turbulent Flames," *Turbulent Reacting Flows*, edited by P. A. Libby and F. A. Williams, Academic Press, London, 1994, Chap. 2, pp. 63–113.

[4]Stahl, G., and Warnatz, J., "Numerical Investigation of Time-Dependent Properties and Extinction of Strained Methane- and Propane-Air Flamelets," *Combustion and Flame*, Vol. 85, No. 3–4, 1991, pp. 285–299.

[5]Darabiha, N., "Transient Behaviour of Laminar Counterflow Hydrogen–Air Diffusion Flames with Complex Chemistry," *Combustion Science and Technology*, Vol. 86, No. 1–6, 1992, pp. 163–181.

[6]Egolfopoulos, F. N., "Dynamics and Structure of Unsteady, Strained, Laminar Premixed Flames," *Proceedings of the Combustion Institute*, Vol. 25, 1994, pp. 1365–1373.

[7]Egolfopoulos, F. N., and Campbell, C. S., "Unsteady Counterflowing Strained Diffusion Flames: Diffusion-Limited Frequency Response," *Journal of Fluid Mechanics*, Vol. 318, July 1996, pp. 1–29.

[8]Rutland, C., and Ferziger, J., "Unsteady Strained Premixed Laminar Flames," *Combustion Science and Technology*, Vol. 73, No. 1–3, 1990, pp. 305–326.

[9]Ghoniem, A. F., Soteriou, M. C., Knio, O. M., and Cetegen, B., "Effect of Steady and Periodic Strain on Unsteady Flamelet Combustion," *Proceedings of the Combustion Institute*, Vol. 24, 1992, pp. 223–230.

[10]Petrov, C., and Ghoniem, A., "The Transient Response of Strained Laminar-Premixed Flames," *Combustion and Flame*, Vol. 102, No. 3, 1995, pp. 401–417.

[11]Im, H. G., Chen, J. H., and Chen, J.-Y., "Chemical Response of Methane Air Diffusion Flames to Unsteady Strain Rate," *Combustion and Flame*, Vol. 118, No. 1–2, 1999, pp. 204–212.

[12]Im, H. G., and Chen, J. H., "Effects of Flow Transients on the Burning Velocity of Laminar Hydrogen/Air Premixed Flames," *Proceedings of the Combustion Institute*, Vol. 28, 2001, pp. 1833–1840.

[13]Cuenot, B., Egolfopoulos, F. N., and Poinsot, T., "An Unsteady Laminar Flamelet Model for Non-Premixed Combustion," *Combustion Theory and Modeling*, Vol. 4, No. 1, 2000, pp. 77–97.

[14]Nguyen, Q.-V., and Paul, P. H., "The Time Evolution of a Vortex–Flame Interaction Observed via Planar Imaging of CH and OH," *Proceedings of the Combustion Institute*, Vol. 26, 1996, pp. 357–364.

[15]Paul, P. H., and Najm, H. N., "Planar Laser-Induced Fluorescence Imaging of Flame Heat Release Rate," *Proceedings of the Combustion Institute*, Vol. 27, 1998, pp. 43–50.

[16]Najm, H. N., and Wyckoff, P. S., "Premixed Flame Response to Unsteady Strain Rate and Curvature," *Combustion and Flame*, Vol. 110, No. 1–2, 1997, pp. 92–112.

[17]Najm, H. N., Knio, O. M., Paul, P. H., and Wyckoff, P. S., "Response of Stoichiometric and Rich Methane–Air Flames to Unsteady Strain Rate and Curvature," *Combustion Theory and Modeling*, Vol. 3, No. 4, 1999, pp. 709–726.

[18]Echekki, T., and Chen, J. H., "Unsteady Strain Rate and Curvature Effects in Turbulent Premixed Methane–Air Flames," *Combustion and Flame*, Vol. 106, No. 1–2, 1996, pp. 184–202.

[19]Echekki, T., Chen, J. H., and Gran, I. R., "The Mechanism of Mutual Annihiliation of Stoichiometric Premixed Methane–Air Flames," *Proceedings of the Combustion Institute*, Vol. 26, 1996, pp. 855–864.

[20]Chen, J. H., Echekki, T., and Kollmann, W., "The Mechanism of Two-Dimensional Pocket Formation in Lean Premixed Methane–Air Flames with Implications to Turbulent Combustion," *Combustion and Flame*, Vol. 116, No. 1–2, 1999, pp. 15–48.

[21]Najm, H. N., Paul, P. H., Knio, O. M., and McIlroy, A., "Transient Response of Premixed Methane–Air Flames," *First MIT Conference on Computational Fluid and Solid Mechanics*, edited by K. J. Bathe, Elsevier, Amsterdam, 2001, pp. 1334–1337.

[22]Petrov, C., and Ghoniem, A. F., "Dynamics and Structure of Interacting Nonpremixed Flames," *Combustion and Flame*, Vol. 115, No. 1–2, 1998, pp. 180–194.

[23]Williams, F. A., *Combustion Theory*, 2nd ed., Addison–Wesley, Reading, MA, 1985, pp. 415–423, 636, 637.

[24]Marzouk, Y. M., Najm, H. N., and Ghoniem, A. F., "Dynamic Response of Strained Premixed Flames to Equivalence Ratio Gradients," *Proceedings of the Combustion Institute*, Vol. 28, 2000, pp. 1859–1866.

[25]Marzouk, Y. M., *The Effect of Flow and Mixture Inhomogeneity on the Dynamics of Strained Flames*, M.S. Thesis, Dept. of Mechanical Engineering, Massachusetts Inst. of Technology, Cambridge, MA, Sept. 1999.

[26]Knio, O. M., Shi, X., and Ghoniem, A. F., "Lagrangian Simulation of a Thin Non-Premixed Flame in the Field of an Asymmetric Layer," *Combustion and Flame*, Vol. 106, No. 1–2, 1996, pp. 41–61.

[27]Petrov, C., and Ghoniem, A., "Numerical Simulation of Reacting Flow with Multi-Step Chemistry," AIAA Paper 97-0291, Jan. 1997.

[28]Petrov, C., "Numerical Simulation of Reacting Flows with Complex Chemistry Using Flame Embedding," Ph.D. Dissertation, Dept. of Mechanical Engineering, Massachusetts Inst. of Technology, Cambridge, MA, Feb. 1997.

[29]Poinsot, T., Veynante, D., and Candel, S., "Diagrams of Premixed Turbulent Combustion Based on Direct Simulation," *Proceedings of the Combustion Institute*, Vol. 23, 1990, pp. 613–619.

[30]Kee, R. J., Dixon-Lewis, G., Warnatz, J., Coltrin, M. E., and Miller, J. A., "A Fortran Computer Code Package for the Evaluation of Gas-Phase Multicomponent Transport Properties," Sandia National Labs., TR SAND86-8246, Livermore, CA, Dec. 1986.

[31]Kee, R. J., Rupley, F. M., Meeks, E., and Miller, J. A., CHEMKIN-III: "A Fortran Chemical Kinetics Package for the Analysis of Gas-Phase Chemical and Plasma Kinetics," Sandia National Labs., TR SAND96-8216, Livermore, CA, May, 1996.

[32]Smooke, M. D., Puri, I. K., and Seshadri, K., "A Comparison Between Numerical Calculations and Experimental Measurement of the Structure of a Counterflow Diffusion Flame Burning Diluted Methane in Diluted Air," *Proceedings of the Combustion Institute*, Vol. 21, 1986, pp. 1783–1792.

[33]Kee, R. J., Grcar, J. F., Smooke, M. D., and Miller, J. A., "A Fortran Program for Modeling Steady Laminar One-Dimensional Premixed Flames," Sandia National Labs., TR SAND85-8240, Livermore, CA, Dec. 1985.

[34]Pernice, M., and Walker, H. F., "NITSOL: A Newton Iterative Solver for Nonlinear Systems," *SIAM Journal on Scientific Computing*, Vol. 19, No. 1, 1998, pp. 302–318.

[35]Eisenstat, S. C., and Walker, H. F., "Globally Convergent Inexact Newton Methods," *SIAM Journal on Optimization*, Vol. 4, No. 2, 1994, pp. 393–422.

[36]van der Vorst, H. A., "Bi-CGSTAB: A Fast and Smoothly Converging Variant of Bi-CG for the Solution of Nonsymmetric Linear Systems," *SIAM Journal on Scientific Computing*, Vol. 13, No. 2, 1992, pp. 631–644.

[37]Saad, Y., *Iterative Methods for Sparse Linear Systems*, PWS Publishing, Boston, 1996.

[38]Najm, H. N., Paul, P. H., Mueller, C. J., and Wyckoff, P. S., "On the Adequacy of Certain Experimental Observables as Measurements of the Flame Burning Rate," *Combustion and Flame*, Vol. 113, No. 3, 1998, pp. 312–332.

[39]Najm, H. N., and Wyckoff, P. S., and Knio, O. M., "A Semi-Implicit Numerical Scheme for Reacting Flow I. Stiff Chemistry," *Journal of Computational Physics*, Vol. 143, No. 2, 1998, pp. 381–402.

[40]Knio, O. M., Najm, H. N., and Wyckoff, P. S., "A Semi-Implicit Numerical Scheme for Reacting Flow II. Stiff Operator-Split Formulation," *Journal of Computational Physics*, Vol. 154, No. 2, 1999, pp. 428–467.

[41]Najm, H. N., Paul, P. H., McIlroy, A., and Knio, O. M., "A Numerical and Experimental Investigation of Premixed Methane–Air Flame Transient Response," *Combustion and Flame*, Vol. 125, No. 1–2, 2001, pp. 879–892.

[42]Im, H. G., Bechtold, J. K., and Law, C. K., "Response of Counterflow Premixed Flames to Oscillating Strain Rates," *Combustion and Flame*, Vol. 105, No. 3, 1996, pp. 358–372.

[43]Sardi, K., Taylor, A. M. K. P., and Whitelaw, J. H., "Extinction of Turbulent Counterflow Flames Under Periodic Strain," *Combustion and Flame*, Vol. 120, No. 3, 2000, pp. 265–284.

[44]Lutz, A. E., Kee, R. J., Grcar, J. F., and Rupley, F. M., "OPPDIF: A Fortran Program for Computing Opposed-Flow Diffusion Flames," Sandia National Labs., TR SAND96-8243, Livermore, CA, May 1997.

[45]Kee, R. J., Miller, J. A., Evans, G. H., and Dixon-Lewis, G., "A Computational Model of the Structure and Extinction of Strained Opposed-Flow Premixed Methane–Air Flames," *Proceedings of the Combustion Institute*, Vol. 22, 1998, pp. 1479–1494.

[46]Dixon-Lewis, G., "Structure of Laminar Flames," *Proceedings of the Combustion Institute*, Vol. 23, 1990, pp. 305–324.

S. K. Aggarwal
Associate Editor